Physics Letters B 781 (2018) 290–294

Contents lists available at ScienceDirect

Physics Letters B

www.elsevier.com/locate/physletb

CP-odd Higgs boson production in $e\gamma$ collisions

Ken Sasaki [a], Tsuneo Uematsu [b,c,*]

[a] Dept. of Physics, Faculty of Engineering, Yokohama National University, Yokohama 240-8501, Japan
[b] Institute for Liberal Arts and Sciences, Kyoto University, Kyoto 606-8501, Japan
[c] Maskwa Institute, Kyoto Sangyo University, Kyoto 603-8555, Japan

ARTICLE INFO

Article history:
Received 4 December 2017
Received in revised form 13 March 2018
Accepted 3 April 2018
Available online 5 April 2018
Editor: J. Hisano

Keywords:
CP-odd Higgs production
Two-photon fusion
Transition form factor
$e\gamma$-collisions

ABSTRACT

We investigate the CP-odd Higgs boson production via two-photon processes in $e\gamma$ collisions. The CP-odd Higgs boson, which we denote as A^0, is expected to appear in the Two-Higgs Doublet Models (2HDM) as a minimal extension of Higgs sector for which the Minimal Supersymmetric Standard Model (MSSM) is a special case. The scattering amplitude for $e\gamma \to eA^0$ is evaluated at the electroweak one-loop level. The dominant contribution comes from top-quark loops when A^0 boson is rather light and $\tan\beta$ is not large. There are no contributions from the W-boson and Z-boson loops nor the scalar top-quark (stop) loops. The differential cross section for the A^0 production is analyzed.

1. Introduction

After the Higgs boson with mass about 125 GeV was discovered by ATLAS and CMS at LHC [1] and its spin, parity and couplings were examined [2], there has been growing interest in constructing a new accelerator facility, like a linear e^+e^- collider [3], which would offer much cleaner experimental data. Along with e^+e^- collider, other options such as e^-e^-, $e^-\gamma$ and $\gamma\gamma$ colliders have also been discussed. See Refs. [4–8] and the references therein. Each option for colliders will provide interesting topics to study, such as the detailed measurement of the Higgs boson properties and the quest for the new physics beyond the Standard Model (SM). An e^-e^- collider is easier to build than an e^+e^- collider and may stand as a potential candidate before positron sources with high intensity are available. The $e^-\gamma$ and $\gamma\gamma$ options are based on e^-e^- collisions, where one or two of the electron beams are converted to the photon beams.

In our previous papers [9,10], we have studied the SM Higgs boson ($H_{\rm SM}$) production in $e\gamma$ collisions, focusing on the transition form factor of $H_{\rm SM}$ boson [9] and also on the dependence of polarizations of the initial electron and photon beams [10]. In this paper we investigate the production of the CP-odd Higgs boson (A^0), which appears in the 2HDM or in the MSSM [11], in an $e^-\gamma$ collider (Fig. 1). A originally proposed center of mass energy was 500 GeV for an e^+e^- linear collider [3]. In the light of an $e^-\gamma$ collider, we study for a case when A^0 boson is rather light. More specifically, we assume that the A^0 mass is less than 500 GeV. We examine the reaction $e\gamma \to eA^0$ at the one-loop level in the electroweak interaction. Due to the absence of the tree-level ZZA^0 and $W^+W^-A^0$ couplings, the one-loop diagrams which contribute to the reaction are through the $\gamma^*\gamma$-fusion and $Z^*\gamma$-fusion processes. It turns out that the contribution of the $\gamma^*\gamma$-fusion diagrams is far more dominant over the one from the $Z^*\gamma$-fusion diagrams. Thus the A^0 production in $e\gamma$ collisions is well-described by the "so-called" transition form factor [9]. We investigate the Q^2 dependence of the transition form factor and the production cross section.

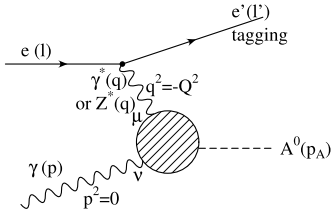

Fig. 1. Production of CP-odd Higgs boson A^0 in the electron–γ collision.

In the next section we briefly outline the CP-odd Higgs boson A^0 in the type-II 2HDM or in the MSSM. In section 3, we calculate the one-loop electroweak corrections to the A^0 production in

* Corresponding author.
E-mail addresses: sasaki@ynu.ac.jp (K. Sasaki), uematsu@scphys.kyoto-u.ac.jp (T. Uematsu).

https://doi.org/10.1016/j.physletb.2018.04.005

$e\gamma$ collisions. We also discuss the transition form factor for the $\gamma^*\gamma$-fusion process in $e\gamma$ scattering. In section 4, we present the numerical analysis of the differential cross section for the A^0 production and its dependence on the A^0 mass. The final section is devoted to the concluding remarks.

2. CP-odd Higgs boson in 2HDM/MSSM

As a minimal extension of the Higgs sector of the SM, we consider the type-II 2HDM which includes the MSSM as a special case [11]. We denote the two $SU(2)_L$ doublets H_1 and H_2 with weak hypercharge $Y=-1$ and $Y=1$, respectively, by the 4 complex scalar fields, ϕ_1^0, ϕ_1^-, ϕ_2^+, ϕ_2^0 as follows:

$$H_1=\begin{pmatrix} H_1^1 \\ H_1^2 \end{pmatrix}=\begin{pmatrix} \phi_1^{0*} \\ -\phi_1^- \end{pmatrix}, \quad H_2=\begin{pmatrix} H_2^1 \\ H_2^2 \end{pmatrix}=\begin{pmatrix} \phi_2^+ \\ \phi_2^0 \end{pmatrix}, \tag{1}$$

where, in the type-II model, H_1 (H_2) couples only to down-type (up-type) quarks and leptons. They acquire the following vacuum expectation values after the spontaneous symmetry breaking:

$$\langle H_1\rangle=\begin{pmatrix} v_1 \\ 0 \end{pmatrix}, \quad \langle H_2\rangle=\begin{pmatrix} 0 \\ v_2 \end{pmatrix}, \quad \tan\beta=v_2/v_1\,. \tag{2}$$

Then 3 degrees of freedom out of 8 consisting of the 4 complex scalar fields are absorbed by the longitudinal components of $W^\pm$, Z, and the remaining 5 degrees of freedom become the following two charged and three neutral physical Higgs bosons:

$$\text{Charged } H^+,\ H^-;\ \text{CP-even } h^0,\ H^0;\ \text{CP-odd } A^0\,. \tag{3}$$

Here we are particularly interested in the CP-odd Higgs boson A^0 and investigate its production in $e\gamma$ collisions.

We enumerate some characteristics of A^0 couplings to other fields in the type-II 2HDM and the MSSM.

1) In contrast to the CP-even Higgs bosons h^0 and H^0, A^0 does not couple to W^+W^- and ZZ pairs at tree level. Hence W-boson and Z-boson one-loop diagrams do not contribute to the A^0 production.
2) A^0 does not couple to other two physical Higgs bosons in cubic interactions.
3) The couplings of A^0 to quarks and leptons are proportional to their masses. Therefore, we consider only the top and bottom quark-loop diagrams for the A_0 production. The A^0 coupling to the top (bottom) with mass m_t (m_b) is given by $\lambda_t\gamma_5$ ($\lambda_b\gamma_5$) with [11]

$$\lambda_t=-\frac{gm_t\cot\beta}{2m_W}\equiv g\widetilde{\lambda}_t m_t, \tag{4}$$

$$\lambda_b=-\frac{gm_b\tan\beta}{2m_W}\equiv g\widetilde{\lambda}_b m_b. \tag{5}$$

Here g and m_W are the weak gauge coupling and the weak boson mass, respectively.
In the MSSM, charginos also couple to A^0. When CP is conserved (which we assume in this paper), the diagonal couplings of A^0 to the chargino mass eigenstates are purely pseudoscalar [12], whose couplings are expressed as $g\kappa_i\gamma_5$ with (see Eq. (4.32) of [12]),

$$\kappa_i=\frac{1}{\sqrt{2}}\Big(\sin\beta U_{i2}V_{i1}+\cos\beta U_{i1}V_{i2}\Big), \qquad i=1,2\,, \tag{6}$$

where U and V are 2×2 orthogonal matrices. Thus $\kappa_i\sim\mathcal{O}(1)$. In the following we deal with two chargino mass eigenstates as a whole and write its coupling to A_0 and mass as κ and m_χ, respectively. We put

$$\lambda_\chi=g\kappa\equiv g\widetilde{\lambda}_\chi m_\chi\,. \tag{7}$$

Recently at LHC, ATLAS [13] and CMS [14] excluded chargino masses below 1140 GeV for the case that the lightest supersymmetric particles are massless [15]. The results depend on the various scenarios for the production and decay of charginos and neutralinos. We therefore take $m_\chi=1$ TeV as a benchmark mass for chargino in this paper.
4) In the case of the MSSM, the trilinear A^0 coupling to mass-eigenstate squark pairs $\tilde{q}_i\tilde{q}_i$ ($i=1,2$) vanishes [11]. Hence, the scalar top-quark (stop) does not contribute to the A^0 production in $e\gamma$ collisions at one-loop level.

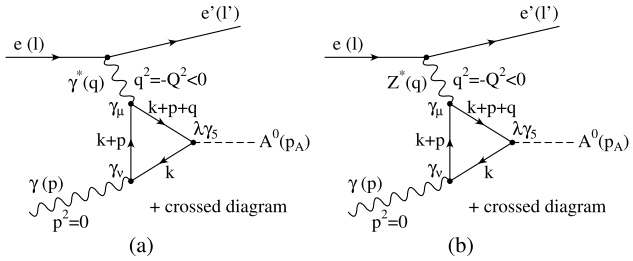

Fig. 2. (a) $\gamma^*\gamma$ fusion diagrams for $e\gamma\to e'A^0$. (b) $Z^*\gamma$ fusion diagrams for $e\gamma\to e'A^0$.

3. CP-odd Higgs boson production in $e\gamma$ collisions

We investigate the production of the CP-odd Higgs boson A^0 in an $e\gamma$ collision experiment (Fig. 1):

$$e(l)+\gamma(p)\to e(l')+A^0(p_A)\,, \tag{8}$$

where we detect the scattered electron in the final state. The one-loop diagrams which contribute to the reaction (8) are classified into two groups: $\gamma^*\gamma$ fusion diagrams and $Z^*\gamma$ fusion diagrams (Fig. 2). As we will see later, the contribution of the former is far more dominant over that of the latter.

Since p is the momentum of a real photon, we have $p^2=0$. We set $q=l-l'$. Assuming that electrons are massless so that $l^2=l'^2=0$, we introduce the following Mandelstam variables:

$$s=(l+p)^2=2l\cdot p, \quad t=(l-l')^2=q^2\equiv-Q^2, \tag{9}$$

$$u=(l-p_A)^2=m_A^2-s-t\,, \tag{10}$$

where $p_A^2=m_A^2$ with m_A being the A^0 boson mass.

3.1. One-loop $\gamma^*\gamma$ fusion diagrams

Due to the characteristics of A^0 couplings to other fields, we take into account only the loops of three fermions (top (t) and bottom (b) quarks and chargino (χ)) for the $\gamma^*\gamma$ fusion diagrams (Fig. 2 (a)). The contribution from the one-loop $\gamma^*\gamma$ fusion diagrams to the scattering amplitude is expressed as

$$\langle e'A^0|T|e\gamma\rangle^f_{\gamma^*\gamma}=[\overline{u}(l')(-ie\gamma_\mu)u(l)]\frac{-i}{q^2+i\epsilon}A^f_{\mu\nu}\epsilon^\nu(p), \tag{11}$$

where $u(l)$ ($\overline{u}(l')$) is the spinor for the initial (scattered) electron with momentum l (l') and $\epsilon^\nu(p)$ is the photon polarization vector with $p_\nu\epsilon^\nu(p)=0$. The tensor $A^f_{\mu\nu}$ with $f=t,b,\chi$ is given as

$$A^f_{\mu\nu}=8N_C^f q_f^2 e^2\lambda_f m_f\varepsilon_{\mu\nu\alpha\beta}q^\alpha p^\beta \times\frac{1}{16\pi^2}C_0(0,q^2,m_A^2;m_f^2,m_f^2,m_f^2), \tag{12}$$

where e is the electromagnetic coupling, N_C^f is a color factor with $N_C^t = N_C^b = 3$, $N_C^\chi = 1$, q_f is a charge factor with $q_t = \frac{2}{3}$, $q_b = -\frac{1}{3}$, $q_\chi = 1$ and C_0 is a Passarino–Veltman three-point scalar integral [16]:

$$C_0(p^2, q^2, (p+q)^2; m_f^2, m_f^2, m_f^2) = \frac{1}{i\pi^2}\int \frac{d^4k}{[k^2 - m_f^2][(k+p)^2 - m_f^2][(k+p+q)^2 - m_f^2]} . \quad (13)$$

The integral C_0 is expressed as the sum of two functions $f(\tau_f)$ and $g(\rho_f)$ as

$$C_0(0, -Q^2, m_A^2; m_f^2, m_f^2, m_f^2) = -\frac{1}{Q^2 + m_A^2}\left\{2f(\tau_f) + \frac{1}{2}g(\rho_f)\right\}, \quad (14)$$

where the dimensionless variables τ_f and ρ_f are defined as

$$\tau_f \equiv \frac{4m_f^2}{m_A^2}, \quad \rho_f \equiv \frac{Q^2}{4m_f^2}, \quad (15)$$

and

$$f(\tau) = \left[\sin^{-1}\sqrt{\frac{1}{\tau}}\right]^2 \qquad \tau \geq 1 , \quad (16)$$

$$= -\frac{1}{4}\left[\log\frac{1+\sqrt{1-\tau}}{1-\sqrt{1-\tau}} - i\pi\right]^2 \qquad \tau < 1 , \quad (17)$$

$$g(\rho) = \left[\log\frac{\sqrt{\rho+1}+\sqrt{\rho}}{\sqrt{\rho+1}-\sqrt{\rho}}\right]^2 . \quad (18)$$

Similar combinations of functions $f(\tau)$ and $g(\rho)$ as in Eq. (14) with the time-like virtual mass, which are different from our space-like case, appear in the Higgs decay processes $H_{\rm SM} \to \gamma^*\gamma$ and $H_{\rm SM} \to Z^*\gamma$ in Ref. [17] (see also Ref. [11] for on-shell decays, $H_{\rm SM} \to \gamma\gamma$ [18] and $H_{\rm SM} \to Z\gamma$).

3.2. Transition form factor

Inserting the expressions of λ_f given in Eqs. (4), (5) and (7) back to Eq. (12), we see that $A_{\mu\nu}^f$ is expressed as

$$A_{\mu\nu}^f = -\frac{e^2 g}{(4\pi)^2} N_C^f q_f^2 \widetilde{\lambda}_f F_f(Q^2, m_A^2, m_f^2)\, \varepsilon_{\mu\nu\alpha\beta} q^\alpha p^\beta , \quad (19)$$

where we have introduced a transition form factor given by

$$F_f(Q^2, m_A^2, m_f^2) = \frac{\tau_f}{1+\rho_f\tau_f}[g(\rho_f) + 4f(\tau_f)] = -8m_f^2 C_0(0, -Q^2, m_A^2; m_f^2, m_f^2, m_f^2). \quad (20)$$

Note that for $m_A < 2m_f$, i.e. $\tau_f > 1$, $f(\tau_f)$ is given by Eq. (16) which is a real function, while for $m_A > 2m_f$, i.e. $\tau_f < 1$ we have $f(\tau_f)$ given by Eq. (17) which is a complex function.

Taking the mass parameters as $m_t = 173$ GeV, $m_b = 4.3$ GeV and $m_\chi = 1000$ GeV, we analyze the behaviors of $|F_f(Q^2, m_A^2, m_f^2)|$. We plot $|F_f(Q^2, m_A^2, m_f^2)|$ in Fig. 3 as a function of m_A for the case $Q^2 = (100)^2$ GeV^2. Note that $|F_f(Q^2, m_A^2, m_f^2)| \to 4$ as $m_f \to \infty$, while $|F_f(Q^2, m_A^2, m_f^2)| \to 0$ as $m_f \to 0$. We see a kink structure at the threshold region $m_A \approx 2m_t$ for $|F_t(Q^2, m_A^2, m_f^2)|$. Fig. 3 shows that the ratio $|F_b(Q^2, m_A^2, m_b^2)|/|F_t(Q^2, m_A^2, m_t^2)| \sim$ 0.003–0.016 and $|F_\chi(Q^2, m_A^2, m_\chi^2)|$ is the same order as $|F_t(Q^2, m_A^2, m_t^2)|$ when $m_\chi = 1000$ GeV.

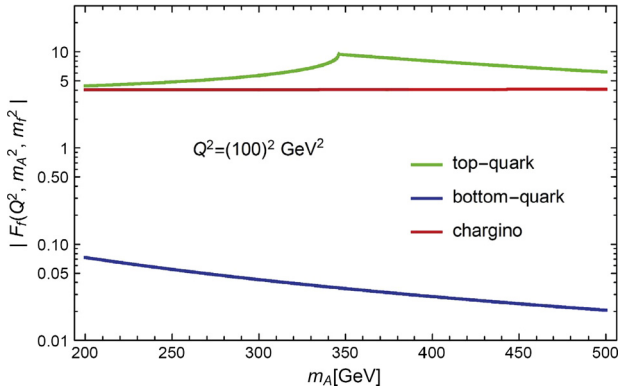

Fig. 3. $|F_f(Q^2, m_A^2, m_f^2)|$ as a function of m_A with $Q^2 = 100^2$ GeV^2: top-quark (green line), bottom-quark (blue line) and chargino with mass $m_\chi = 1000$ GeV (red line). (For interpretation of the colors in the figure(s), the reader is referred to the web version of this article.)

On the other hand, we obtain

$$|N_C^b q_b^2 \widetilde{\lambda}_b|/|N_C^t q_t^2 \widetilde{\lambda}_t| = \frac{\tan^2\beta}{4} , \quad (21)$$

$$|N_C^\chi q_\chi^2 \widetilde{\lambda}_\chi|/|N_C^t q_t^2 \widetilde{\lambda}_t| = \frac{3}{2}\frac{m_W}{m_\chi}|\kappa|\tan\beta . \quad (22)$$

Direct searches for heavy neutral Higgs bosons have been performed at LHC. The results were interpreted in the MSSM benchmark scenarios. In the context of the hMSSM scenario [19], ATLAS data [20] excluded $\tan\beta > 1.0$ for $m_A = 250$ GeV and $\tan\beta > 42.0$ for $m_A = 1.5$ TeV at the 95% CL. Here in this paper we are dealing with a rather light A^0 boson with mass $m_A \leq 500$ GeV. Therefore we consider the case where $\tan\beta$ is not large, e.g. $\tan^2\beta \leq 10$.

The production cross section is proportional to the absolute square of the amplitude. Hence the ratio of the bottom-quark (charginos) contribution to the one of top-quark is given as the square of the quantity in Eq. (21) (Eq. (22)) multiplied by $|F_b|^2/[F_t|^2$ ($|F_\chi|^2/[F_t|^2$). Then we find that for the case $\tan^2\beta \leq 10$ we can ignore the contributions from the bottom-quark and charginos as compared to the one from top-quark. When $\tan\beta \simeq 10$ we can still neglect the bottom-quark contribution but the chargino's contribution becomes the same order as the top-quark contribution.

In the following we proceed with our analysis of the reaction $e\gamma \to eA^0$ assuming that A^0 boson is rather light and $\tan\beta$ is not large.

3.3. One-loop $Z^*\gamma$ fusion diagrams

The one-loop $Z^*\gamma$ fusion diagrams for the A^0 production are obtained from the one-loop $\gamma^*\gamma$ fusion diagrams by replacing the photon propagator with that of the Z boson with mass m_Z (Fig. 2 (b)). The loop contributions from three fermions (top (t) and bottom (b) quarks and chargino (χ)) are expressed in terms of the function $F_f(Q^2, m_A^2, m_f^2)$ in Eq. (20). Since the coupling strengths of $Z \cdot t \cdot t$, $Z \cdot b \cdot b$ and $Z \cdot \chi \cdot \chi$ vertices are the same order of magnitude, the argument in the previous subsection again follows: we can ignore the contributions from the bottom-quark and charginos for the case when A^0 boson is rather light and $\tan\beta$ is not large while the chargino mass is around 1 TeV.

We consider the top quark loop contribution to the $Z^*\gamma$ fusion diagrams and obtain

$$\langle e' A^0 | T | e\gamma \rangle^t_{Z^*\gamma}$$
$$= \frac{g}{4\cos\theta_W}[\bar{u}(l')(i\gamma_\mu)(f_{Ze}+\gamma_5)u(l)]\frac{-i}{q^2-m_Z^2}\widetilde{A}^t_{\mu\nu}\epsilon^\nu(p)\,, \quad (23)$$

with

$$\widetilde{A}^t_{\mu\nu} = 8N_C^t q_t e\frac{g}{4\cos\theta_W}m_t\lambda_t f_{Zt}\epsilon_{\mu\nu\alpha\beta}q^\alpha p^\beta \times\frac{1}{16\pi^2}C_0(0,-Q^2,m_A^2;m_t^2,m_t^2,m_t^2)\,, \quad (24)$$

where f_{Ze} and f_{Zt} are the strength of vector part of the Z-boson coupling to electron and top quark, respectively, and are given by

$$f_{Ze} = -1+4\sin^2\theta_W\,, \qquad f_{Zt} = 1-\frac{8}{3}\sin^2\theta_W\,, \quad (25)$$

with θ_W being the Weinberg angle. In terms of the function F_t given in Eq. (20), $\widetilde{A}^t_{\mu\nu}$ is rewritten as

$$\widetilde{A}^t_{\mu\nu} = -\frac{eg^2N_C^t q_t\widetilde{\lambda}_t f_{Zt}}{(4\pi)^2 4\cos\theta_W}F_t(Q^2,m_A^2,m_t^2)\,\varepsilon_{\mu\nu\alpha\beta}q^\alpha p^\beta \quad (26)$$

3.4. Differential cross section

Adding two amplitudes $\langle e' A^0|T|e\gamma\rangle^t_{\gamma^*\gamma}$ and $\langle e' A^0|T|e\gamma\rangle^t_{Z^*\gamma}$ given in Eqs. (11) and (23), we calculate the differential cross section for the A^0 production in $e\gamma$ collisions with unpolarized initial beams, which turns out to be the sum of three terms:

$$\frac{d\sigma_{(\gamma^*\gamma)}}{dt} = \frac{\alpha_{\rm em}^3}{64\pi}\frac{g^2}{4\pi}\left(\frac{\cot\beta}{2m_W}\right)^2\frac{1}{-t}\left[1+\frac{u^2}{s^2}\right] \times\left|N_C^t q_t^2 F_t(Q^2,m_A^2,m_t^2)\right|^2\,, \quad (27)$$

$$\frac{d\sigma_{(Z^*\gamma)}}{dt} = \frac{\alpha_{\rm em}}{64\pi}\left(\frac{g^2}{4\pi}\right)^3\left(\frac{\cot\beta}{2m_W}\right)^2\left(\frac{1}{16\cos^2\theta_W}\right)^2\frac{-t}{(t-m_Z^2)^2} \times\left[1+\frac{u^2}{s^2}\right]f_{Zt}^2(f_{Ze}^2+1)\left|N_C^t q_t F_t(Q^2,m_A^2,m_t^2)\right|^2\,, \quad (28)$$

$$\frac{d\sigma_{(\rm interference)}}{dt} = -2\times\frac{\alpha_{\rm em}^2}{64\pi}\left(\frac{g^2}{4\pi}\right)^2\left(\frac{\cot\beta}{2m_W}\right)^2\frac{1}{16\cos^2\theta_W}\frac{-1}{t-m_Z^2} \times\left[1+\frac{u^2}{s^2}\right]f_{Zt}f_{Ze}q_t\left|N_C^t q_t F_t(Q^2,m_A^2,m_t^2)\right|^2\,, \quad (29)$$

where each corresponds to the contribution of the $\gamma^*\gamma$ fusion diagrams, the $Z^*\gamma$ fusion diagrams and their interference, respectively, and $\alpha_{\rm em} = e^2/4\pi$.

4. Numerical analysis

We analyze numerically the three differential cross sections given in Eqs. (27)–(29). We choose the mass parameters and the coupling constants as follows:

$$m_t = 173\ \text{GeV}\,, \quad m_Z = 91\ \text{GeV}\,, \quad m_W = 80\ \text{GeV}\,,$$
$$\cos\theta_W = \frac{m_W}{m_Z}\,, \quad e^2 = 4\pi\alpha_{em} = \frac{4\pi}{128}\,, \quad g = \frac{e}{\sin\theta_W}\,. \quad (30)$$

The electromagnetic constant e^2 is chosen to be the value at the scale of m_Z. From Eqs. (25) and (30), we find $f_{Zt}f_{Ze} < 0$ and, therefore, Eq. (29) shows that the interference between the $\gamma^*\gamma$ and $Z^*\gamma$ fusion diagrams works constructively and $\frac{d\sigma_{(\rm Interference)}}{dt}$ is positive.

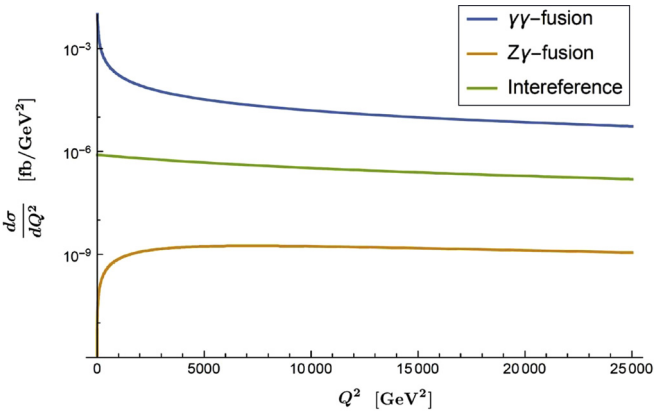

Fig. 4. Comparison of the contribution among three differential cross sections for $\sqrt{s} = 500$ GeV, $m_A = 400$ GeV and $\cot\beta = 1$.

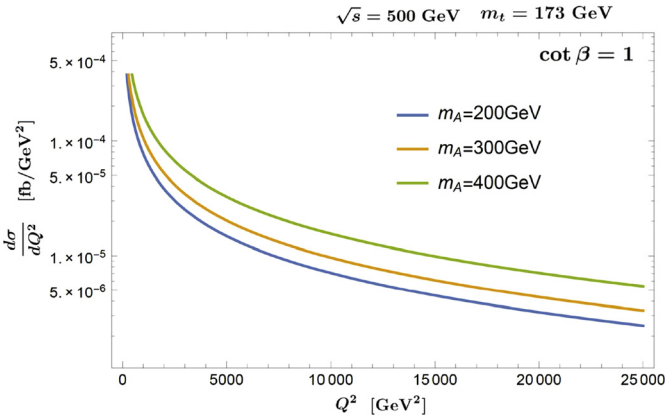

Fig. 5. Differential cross section for the production of CP-odd Higgs boson A^0 with mass $m_A = 200,\ 300,\ 400$ GeV.

We plot these differential cross sections as a function of Q^2 in Fig. 4 for the case $\sqrt{s} = 500$ GeV, $m_A = 400$ GeV and $\cot\beta = 1$. (In fact, the cross sections are proportional to $\cot^2\beta$.) We find that the contribution from the $\gamma^*\gamma$ fusion diagrams is far more dominant over those from $Z^*\gamma$-fusion diagrams as well as from the interference term. Actually we observe that at $Q^2 = 1000$ (5000) GeV^2, the ratio of $\frac{d\sigma_{(Z^*\gamma)}}{dQ^2}$ to $\frac{d\sigma_{(\gamma^*\gamma)}}{dQ^2}$ is 4.3×10^{-6} (5.2×10^{-5}) and $\frac{d\sigma_{(\rm Interference)}}{dQ^2}$ to $\frac{d\sigma_{(\gamma^*\gamma)}}{dQ^2}$ is 4.1×10^{-3} (1.4×10^{-2}). Thus the A^0 production in $e\gamma$ collisions is well-described by the $\gamma^*\gamma$ fusion diagrams with the top quark loop. This means that the transition form factor of the A^0 boson defined as $N_C^t q_t^2 F_t(Q^2,m_A^2,m_t^2)$ in Eq. (20) indeed makes sense and may be measurable in $e\gamma$ collider experiments.

Now we shall focus on the $\gamma^*\gamma$ fusion process based on the formula for the production cross section given in Eq. (27). In Fig. 5 we plot the differential production cross section of A^0 with mass $m_A = 200,\ 300,\ 400$ GeV for the case $\sqrt{s} = 500$ GeV and $\cot\beta = 1$. We find that for this kinematical region the production cross section for A^0 increases as m_A gets larger, which looks somewhat unexpected at first glance. We examine this behavior in more detail by computing the mass dependence of the differential cross section. We plot in Fig. 6 the dependence of the differential cross section $d\sigma/dQ^2$ on the A^0 boson mass with $Q^2 = (80)^2$, $(90)^2$ and $(100)^2$ GeV^2 for the case $\sqrt{s} = 500$ GeV and $\cot\beta = 1$. We see

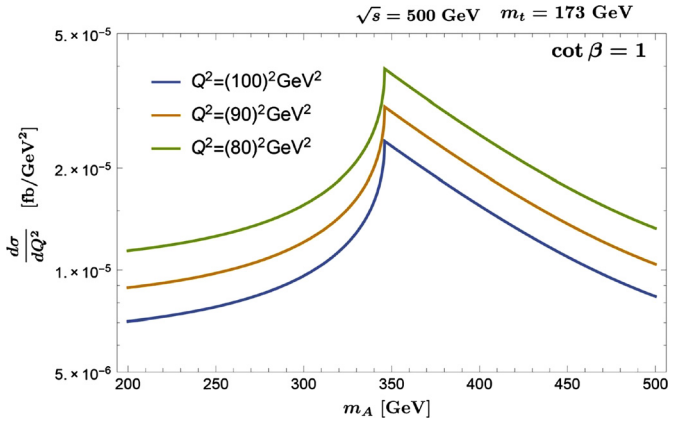

Fig. 6. The A^0 mass dependence of the differential cross section with $Q^2 = (80)^2$ GeV^2, $(90)^2$ GeV^2, $(100)^2$ GeV^2.

that, in the region $m_A < 2m_t$, the differential cross section $d\sigma/dQ^2$ with fixed Q^2 increases along with m_A. When m_A goes beyond $2m_t$, it turns to decrease. We observe the strong kink structure corresponding to the threshold effect at $m_A = 2m_t \approx 346$ GeV (see Eqs. (16) and (17)).

5. Summary and discussion

In this paper we have investigated the production of the CP-odd Higgs boson A^0 which appears in the type-II 2HDM and the MSSM through $e\gamma$ collisions. In contrast to the SM Higgs boson H_{SM} or the CP-even Higgs boson h^0 and H^0, the A^0 boson does not couple to W^+W^- and ZZ pairs because of the CP-odd nature. Hence W-boson and Z-boson loop diagrams do not contribute to the A^0 production at one-loop level.

The A^0 production arises via $\gamma^*\gamma$ fusion or via $Z^*\gamma$ fusion processes. It has turned out that because of the smallness of the e–e–Z and Z–t–t couplings as well as the Z boson propagator, the contribution from the $\gamma^*\gamma$ fusion diagrams is far more dominant over that from $Z^*\gamma$ fusion. Thus, in effect, we have to consider only the photon-exchange diagrams, and it makes sense to introduce the transition form factor of the A^0 boson.

Up to the electroweak one-loop order, the top quark triangle diagrams are only relevant for the production of the A^0 boson when A^0 boson is rather light and $\tan\beta$ is not large. There is no scalar top-quark (stop) contribution. Thus the production amplitude as well as the transition form factor show much simpler structure compared with those of the SM Higgs boson or the CP-even Higgs bosons.

When the mass of the A^0 boson, m_A is smaller than $2m_t$ the transition form factor is a real function of Q^2, while if m_A is larger than $2m_t$, the transition form factor becomes complex. The production cross section of the A^0 boson is given by the absolute square of the transition form factor together with some kinematical factors.

For a fixed value of m_A, the differential production cross section shows a decreasing function of Q^2. On the other hand, if we fix Q^2 and vary the mass of A^0, it increases as m_A for $m_A < 2m_t$ and decreases for $m_A > 2m_t$. This feature is common with the total cross section.

References

[1] ATLAS Collaboration, Phys. Lett. B 716 (2012) 1;
CMS Collaboration, Phys. Lett. B 716 (2012) 30.
[2] ATLAS Collaboration, Phys. Lett. B 726 (2013) 88;
ATLAS Collaboration, Phys. Lett. B 726 (2013) 120;
CMS Collaboration, Phys. Rev. Lett. 110 (2013) 081803.
[3] http://www.linearcollider.org.
[4] A. De Roeck, Physics at a $\gamma\gamma$, $e\gamma$ and e^-e^- option for a linear collider, arXiv:hep-ph/0311138, 2003.
[5] V.I. Telnov, Nucl. Instrum. Methods A 455 (2000) 63, arXiv:hep-ex/0001029;
B. Badelek, et al., Int. J. Mod. Phys. A 19 (2004) 5097, arXiv:hep-ex/0108012;
M.M. Velasco, et al., eConf C010630 (2001) E3005, arXiv:hep-ex/0111055.
[6] M. Melles, W.J. Stirling, V.A. Khoze, Phys. Rev. D 61 (2000) 054015;
M. Melles, Nucl. Phys. Proc. Suppl. 82 (2000) 379;
G. Jikia, S. Soldner-Rembold, Nucl. Phys. Proc. Suppl. 82 (2000) 373;
M.M. Mühlleitner, M. Krämer, M. Spira, P.M. Zerwas, Phys. Lett. B 508 (2001) 311;
M.M. Mühlleitner, Acta Phys. Pol. B 37 (2006) 1127, arXiv:hep-ph/0512232;
D.M. Asner, J.B. Gronberg, J.F. Gunion, Phys. Rev. D 67 (2003) 035009;
S.J. Brodsky, Int. J. Mod. Phys. A 20 (2005) 7306;
P. Niezurawski, eConf C050318 (2005) 0503.
[7] S.A. Bogacz, et al., SAPPHiRE: a small $\gamma\gamma$ Higgs factory, arXiv:1208.2827 [physics.acc-ph], 2012.
[8] I.F. Ginzburg, M. Krawczyk, Testing Higgs physics at the photon collider, arXiv:1310.5881 [hep-ph], 2013;
I.F. Ginzburg, M.V. Vychugin, Phys. At. Nucl. 67 (2004) 281.
[9] N. Watanabe, Y. Kurihara, K. Sasaki, T. Uematsu, Phys. Lett. B 728 (2014) 202;
N. Watanabe, Y. Kurihara, K. Sasaki, T. Uematsu, PoS (RADCOR 2013) 050;
N. Watanabe, Y. Kurihara, K. Sasaki, T. Uematsu, PoS (RADCOR 2013) 053;
N. Watanabe, Y. Kurihara, K. Sasaki, T. Uematsu, PoS (QFTHEP 2013) 040.
[10] N. Watanabe, Y. Kurihara, T. Uematsu, K. Sasaki, Phys. Rev. D 90 (2014) 033015.
[11] J.F. Gunion, H.E. Haber, G. Kane, S. Dawason, The Higgs Hunter's Guide, Addison–Wesley, 1990.
[12] J.F. Gunion, H.E. Haber, Nucl. Phys. B 272 (1986) 1.
[13] ATLAS Collab., ATLAS-CONF-2017-039, 2017.
[14] CMS Collab., arXiv:1709.05406, 2017.
[15] C. Patrignani, et al., Particle Data Group, Chin. Phys. C 40 (2016) 100001 and 2017 update. 113. Supersymmetry, Part II (Experiment).
[16] G. Passarino, M. Veltman, Nucl. Phys. B 160 (1979) 151;
G. 't Hooft, M.J.G. Veltman, Nucl. Phys. B 153 (1979) 365;
G.J. van Oldenborgh, J.A.M. Vermaseren, Z. Phys. C 46 (1990) 425.
[17] J.C. Romao, S. Andringa, Eur. Phys. J. C 7 (1997) 631.
[18] J. Ellis, M.K. Gaillard, D.V. Nanopoulos, Nucl. Phys. B 106 (1976) 292;
B.L. Ioffe, V.A. Khoze, Sov. J. Part. Nucl. 9 (1978) 50;
M.A. Shifman, A.I. Vainshtein, M.B. Voloshin, V.I. Zakharov, Sov. J. Nucl. Phys. 30 (1979) 711;
M.A. Shifman, A.I. Vainshtein, M.B. Voloshin, V.I. Zakharov, Phys. Rev. D 85 (2012) 013015;
T.G. Rizzo, Phys. Rev. D 22 (1980) 178;
M.B. Gavela, G. Girardi, C. Malleville, P. Sorba, Nucl. Phys. B 193 (1981) 257;
W.J. Marciano, C. Zhang, S. Willenbrock, Phys. Rev. D 85 (2012) 013002.
[19] A. Djouadi, et al., Eur. Phys. J. C 73 (2013) 2650;
E. Bagnaschi, et al., LHCHXSWG-2015-002, CERN, 2015.
[20] ATLAS Collab., J. High Energy Phys. 01 (2018) 055.